Available online at www.sciencedirect.com
ScienceDirect
Polymer 48 (2007) 5734–5741
polymer
www.elsevier.com/locate/polymer

Nanostructural features in silica–polyvinyl acetate nanocomposites characterized by small-angle scattering

R. Aravinda Narayanan [a], P. Thiyagarajan [b,*], Ai-Jun Zhu [c], Benjamin J. Ash [c], M.L. Shofner [c], Linda S. Schadler [c], Sanat K. Kumar [c], S.S. Sternstein [c,*]

[a] *Chemical Sciences Division, Oak Ridge National Laboratory, Oak Ridge, TN 37831, USA*
[b] *Intense Pulsed Neutron Source Division, Argonne National Laboratory, Argonne, IL 60439, USA*
[c] *Materials Science and Engineering Department, Rensselaer Polytechnic Institute, Troy, NY 12180, USA*

Received 19 April 2007; received in revised form 12 July 2007; accepted 13 July 2007
Available online 28 July 2007

Abstract

Small-angle scattering (SAS) experiments were carried out on nanocomposites of poly(vinyl acetate) (PVAc) and fumed silica nanoparticles with different surface areas and chemical treatment, in the wave-vector (Q) range: 0.0002–1 $Å^{-1}$. SAS data on composites with matrices of two different molecular weights indicate that the particle aggregation is independent of the molecular weight of the matrix for a fixed filler concentration and surface treatment. Particle size distributions derived from the SAS data suggest that particle aggregation is reduced when the native surface hydroxyl groups are blocked by various surface treatments, which also reduce the bonding strength to the polymer matrix. The unified exponential/power-law analysis of the SAS data shows three levels of hierarchy in the organization of silica particles. The first level consists of small aggregates of silica particles. At the second level we observe polydispersed aggregates resembling mass-fractal objects that is corroborated by TEM. The polydispersed aggregates further associate to form agglomerates at the third level. The relevance of these findings to the mechanism of nanofiller reinforcement of linear amorphous polymers above T_g is discussed.
© 2007 Elsevier Ltd. All rights reserved.

Keywords: Nanocomposites; Reinforcement; Small-angle scattering

1. Introduction

It is generally accepted that nanofillers reinforce polymers more effectively than conventional (micron size) fillers, albeit by mechanisms that are controversial and elusive. Traditional polymer composites filled with micron size inorganic fillers often show improved modulus and yield strength, and a corresponding increase in heat distortion temperature. However, these gains are often accompanied by losses in ductility and toughness. In recent years, composites prepared with nanoscale fillers have provided the ability to increase the modulus, but without the corresponding loss of toughness. Often, the modulus and other property enhancements are achieved at very low filler volume fractions [1].

Crucial to understanding the mechanical properties of nanocomposites is the recognition that nanoscale fillers have an inherently high surface area to volume ratio leading to large interfacial area between the filler and matrix. This has led investigators [2,3] to suggest that there is an interaction zone (IZ) surrounding each filler particle with substantially altered physical properties relative to the neat polymer matrix such as higher or lower polymer mobility, altered chemical crosslinking or entanglement density, and altered glass transition temperature (T_g) or modulus.

However, the addition of nanoparticles brings along other issues as well. Increased interaction of the nanoparticle with the polymer also affects its interaction with other

* Corresponding authors.
E-mail addresses: thiyaga@anl.gov (P. Thiyagarajan), sterns@rpi.edu (S.S. Sternstein).

0032-3861/$ - see front matter © 2007 Elsevier Ltd. All rights reserved.
doi:10.1016/j.polymer.2007.07.049

nanoparticles, often leading to the formation of particle aggregates and agglomerates, which is usually detrimental to property enhancements. Some models explaining the mechanical behavior of polymer nanocomposites do consider the effect of particle aggregation. Nonlinear viscoelastic behavior of filled elastomers is an example. The reduction of dynamic storage modulus in filled elastomers with increasing strain amplitude, a nonlinear viscoelastic behavior known as the Payne effect [4], is understood as due to the breakage of particle agglomerates with increasing strain [5]. There are problems with this explanation. While agglomeration has to play an important role, especially when the polymer–filler interaction is repulsive or is not strongly attractive, how do we understand the nonlinear viscoelastic behavior of filled elastomers and melts and the filler reinforcement, in cases where the filler and the polymer are attracted to each other [6–9]?

Other related features that defy explanation are the following: (1) the reinforcement obtained at relatively low volume fractions of filler can be from 10 to 30 times what is predicted from standard micromechanical models such as the Mori–Tanaka theory; (2) the kinetics of the modulus recovery process following large strain perturbations is not readily explained or accounted for by any known re-agglomeration theory [8]. This was the motivation for our recent study of the nonlinear viscoelastic properties of nanosilica filled poly(vinyl acetate) (PVAc) melts (no chemical crosslinking) by Sternstein and Zhu that supports an alternative mechanism in which filler–polymer interactions determine the nonlinear behavior of the dynamic modulus [7]. This study examined the effects of various filler concentrations and surface treatments on the dynamic moduli of the composite materials over a wide range of strain amplitudes. Key results of this study were the following: The shape of the loss factor curve, the ratio of loss modulus to the storage modulus, with varying strain was found to be specific to filler surface treatment regardless of the filler concentration [7]. These composites displayed attributes of either reinforced (filled) solids or reinforced viscous liquids depending on the filler surface treatment and the strain amplitude (and history) at which the measurements were made, for a given temperature. The evidence clearly suggests that the matrix phase behavior is altered in the presence of nanofillers. In this regard, it has been proposed [7] that the restrictions in chain conformational states associated with the labile bonding of polymer segments to the filler surface play a crucial role in the reinforcement mechanism, with the applied stress, temperature and frequency of measurement serving to alter the kinetics of the chain reconfigurations at and near the filler surface.

In all these processes, the roles of filler aggregation and deaggregation are crucial, since they would also be dependent on similar external stimuli and serve to constrain the spatial dimensions occupied by the matrix polymer, an especially important consideration at higher volume fractions of filler. This is the motivation for the present study in which the aggregation state of the nanoparticles in silica–PVAc nanocomposites is characterized with varying nanoparticle–polymer interactions. Elucidating the arrangement of nanoparticles in polymer nanocomposites is a challenge in its own right, and very few comprehensive studies exist. Transmission electron microscopy is a widely used technique, in this context. However, SAS has the advantage that it samples a larger volume and provides a statistical picture of the particle distribution.

2. Experimental

The nanocomposites were prepared using a method described in detail elsewhere [7]. Briefly, the PVAc, obtained from Aldrich at various molecular weights, was dissolved in acetone. Untreated (NT) fumed silica fillers (as received) were obtained from Aldrich having a surface area of 380 m^2/g and from Cabot having surface areas of 200 and 100 m^2/g. The average fundamental particle radii quoted by the manufacturer for the particles are 35, 65 and 135 Å, respectively. Several surface treated fillers (ST) were also obtained from Cabot. The appropriate filler was mixed with the polymer solution followed by ultrasonication to ensure good dispersion. A cooling bath was used to maintain a constant temperature and a sonicator spreader horn was employed to avoid intense sonic energy and cavitation at the probe tip thereby avoiding degradation of the polymers. The solvent was then evaporated at room temperature and the resulting nanocomposite was dried in a vacuum oven at ca. 60 °C. The composite was then quenched with liquid nitrogen to facilitate grinding into a powder and further dried in the vacuum oven at 110 °C to ensure complete solvent removal. The powder was used to mold samples for scattering measurements. Composites of both non-treated (NT) and surface treated (ST) fillers were made. The non-treated silica surface contains hydroxyl groups that form hydrogen bonds with the acetate groups of the matrix polymer. The surface treatment of silica is essentially to prevent this hydrogen bonding by reacting the surface with a small organic group (S) such as hexamethyldisilizane (HMDS) or dimethyldichlorosilane (DMDCS) or long tethered polymer chains (L) of polydimethylsiloxane (PDMS). In the present study two filler concentrations that are below the percolation threshold for spheres, 2.5 and 12.5 vol.%, were investigated. Two MW polymers were used as the matrix material, namely 83 and 140 kDa.

The structural features of nanoparticles in the nanocomposites were characterized using ultra small-angle X-ray scattering at UNICAT (33-ID, Advanced Photon Source) and SANS at SAND (Intense Pulsed Neutron Source) of Argonne National Laboratory. The range of the scattering wave-vector (Q), defined as $Q = 4\pi \sin\theta/\lambda$, ($\lambda$ is the wavelength of the probe and 2θ is the scattering angle) probed at the SAND instrument [10] is 0.0035–1.0 $Å^{-1}$, and at UNICAT [11] 0.0002–0.5 $Å^{-1}$.

2.1. Small-angle scattering

Small-angle scattering [12] measures density fluctuations in a length scale of 1–1000 nm. In complex systems containing aggregates of nanoparticles and their agglomerates this technique enables characterization of the hierarchical structures and provides the particle size distribution. The absolute

scattered intensity from a small-angle scattering measurement is related to the particle form factor – $P(Q)$, and the structure factor – $S(Q)$,

$$I(Q) = N_p V_p^2 (\rho_{Part} - \rho_{Poly})^2 P(Q) S(Q) \quad (1)$$

where N_p is the number density of particles, V_p is the volume of the particle, ρ_{Part} and ρ_{Poly} are the scattering length densities of the nanoparticle and the polymer, respectively. In the present case, the observed intensity arises from the chemical and density fluctuations due to different levels of aggregates of silica particles in the PVAc matrix. In a dilute system such as the composites with 2.5 vol.% fillers, it is reasonable to assume that inter-particle correlations will be very small and therefore, $S(Q)$ can be assumed to be 1. However, for samples with 12.5 vol.% fillers, we can identify strong inter-particle correlations in the organization of agglomerates in the ultra low Q region of the USAXS data. Interestingly, the scattering data at $Q > 0.004$ Å^{-1} scales well with the filler concentration and hence could still be used to derive the particle size distribution from a nonlinear least-square fit. However, to investigate the structural features in a wider length scale we use the USAXS data for samples with 2.5 vol.% fillers to extract the particle size distribution and the hierarchical organization of the particles from a unified fit [13] described below.

2.2. Unified fit analysis of small-angle scattering

When hierarchical structures are present the question arises as to how the particles are organized at each level and how they correlate in terms of polydispersity or fractal scaling, if any. Such information can be derived using the unified fit analysis [13] of the small-angle scattering data. At each level, contributions to $P(Q)$ in Eq. (1) can be used to derive a z-average R_g from a Q region where $Q_{max}R_g \sim 1$ using the Guinier law,

$$I(Q) = G\exp\left(-\frac{Q^2R_g^2}{3}\right) \quad (2)$$

and a power-law exponent (P) from the power-law

$$I(Q) \sim Q^{-P}, \quad (3)$$

obeyed in the Q region where $QR_g \gg 1$. The value of P can be used to interpret the shape of the particles or the fractal nature of the aggregates or agglomerates [12,14]. In the case of mass fractals, P relates to mass, M, and length, R, as $M \sim R^P$ and P assumes non-integer values between 1 and 3 depending on the density of particles in the aggregate or agglomerate. On the other hand, for a particle with a distinct surface, the scattering arising from the surface of the particle leads to the following intensity variation:

$$I(Q) \sim Q^{D_S-6} \quad (4)$$

where D_s is the *surface fractal* dimension [12] and is based on the relation between surface area (S) and the sphere radius (R) – $S \sim R^{D_s}$: D_s is a measure of the roughness of the surface, and varies between 2 and 3, which corresponds to a power-law slope P between 3 and 4 at $QR_g \gg 1$. Note that $D_s = 2$ or $P = 4$ pertains to the smooth surface as shown by Porod [15].

It is clear from the above discussion that $P(Q)$ at each level of the hierarchy can be represented by a combination of exponential and power-law regions. This is the basic motivation of the unified fit approach [13,16] to small-angle scattering which has been used to fit the data in the present work and whose functional form for systems with hierarchical structure is given below.

$$I(Q) = \sum_{i=1}^{n}\left(G_i\exp\left(-Q^2R_{g_i}^2/3\right) + B_i\exp\left(-Q^2R_{g_{i-1}}^2/3\right) \times\left\{\left[erf\left(QR_{g_i}/6^{1/2}\right)\right]^3/Q\right\}^{P_i}\right) + \gamma \quad (5)$$

Here $i = 1$ refers to the smallest-size structural level and γ is the flat background scatter. G_i is the Guinier prefactor and is related to the average particle volume [16], V_p, through the relationship $G_i = N_p r_e^2 (\rho_{Part} - \rho_{Poly})^2 V_p^2$; r_e is the classical electron radius. B_i is the power-law prefactor and is related to the average surface area [16], S_p, of the particle via the relation: $B_i = 2\pi r_e^2 N_p (\rho_{Part} - \rho_{Poly})^2 S_p$. It is important to note that the structure at various levels influence each other, and therefore, the final values of the parameters, G_i, R_{gi}, B_i, and P_i are obtained by least-square fitting of the entire data after determining the values by *local* fitting at each level. From these parameters a number of structural characteristics of the particles and their arrangement can be obtained apart from R_{gi} and P. A couple of parameters relevant to this study are: (1) the aggregate polydispersity index [17], $A = B_i R_{gi}^{P_i}/P_i\Gamma(P_i/2)G_i$, where $\Gamma()$ is the Gamma function. If $A = 1$, it implies the presence of linear monodispersed aggregates. If $A < 1$, it corresponds to branched monodispersed aggregates, and if $A > 1$, it implies the presence of linear polydispersed aggregates. (2) The particle surface area to volume ratio, A_p/V_p, provided the particle scattering follows the Porod law, i.e., $P_i = 4$.

2.3. Transmission electron microscopy

In order to complement the USAXS data on hierarchical structures, image analysis was performed on TEM images of the 2.5 vol.% NT-380/PVAc (83 kDa) composite. Thin sections of the material were prepared using a RMC PowerTome XL Ultramicrotome with a cryogenic accessory. The samples were sectioned at −50 °C using a glass knife. The imaging was done at several magnifications with a Phillips CM-12 TEM operating at an acceleration voltage of 120 kV. The image negatives were scanned at 1200 pixels/inch and analyzed using ImageJ, a public domain image-processing program available from the National Institutes of Health. Three quantities were determined in the image analysis to compare with the scattering data: the radial profile of the images' Fast Fourier Transform (FFT), the fractal dimension, and the average particle size. The FFT was performed using the integrated program contained in ImageJ and a radial profile was

used to obtain the pixel intensity information as a function of frequency. The second parameter, fractal dimension, was determined by using a box counting procedure. In this method, a grid was applied to the image, and the number of grid boxes that the boundary passes through was counted. The procedure was repeated with different grid sizes. The number of grid boxes was plotted against the grid size in a log–log plot, and the slope of this line represented the fractal dimension. Finally, the particle size was measured with threshold images using the automatic settings. The particle size was calculated as the equivalent radius from the average particle area assuming that the aggregate shape was spherical. Objects with an equivalent radius less than 35 Å were excluded from the average so as not to count background features as particles.

3. Results and discussion

Fig. 1(a) shows the SANS data of composites with NT-380 filler (untreated surface) in PVAc for two different MW matrices, 83 and 140 kDa, and two different filler concentration levels, namely 2.5 and 12.5 vol.% while Fig. 1(b) shows the data for the ST-200S filler (surface treated with hexamethyldisilazane) composites, for the same two MW matrices and concentration levels. The intensity at the high Q region in the normalized SANS data corresponds to the incoherent scattering from the hydrogen atoms in the polymer. The scattering intensity which increases steeply at $\sim Q < 0.1$ Å^{-1} is from aggregates of the nanoparticles. As expected, the intensities are greater at higher filler concentration. The scattering data for composites with ST-200S have similar shapes at 2.5 and 12.5 vol.% filler loadings, but for the composites containing NT 380 they differ in the low Q region. Interestingly, for a given concentration and filler type, the scattering data remains the same for different MW polymer matrices. Therefore, changes in reinforcement level with matrix molecular weight cannot be ascribed to differences in filler aggregation, for a given filler type and concentration, as noted previously [7].

A general feature in all the experimental log $I(Q)$ versus log Q curves in Figs. 1–4 is the presence of a gentle knee at $Q \sim 0.01$ Å^{-1} that signifies that the scattering is produced by a particle of a defined size ($R_g \sim 1/Q$). However, the Q values corresponding to the knee are lower than those expected for the quoted sizes of 35, 65 and 135 Å for the particles with surface areas 380, 200, and 100 m^2/g, respectively. Theoretically calculated form factors [$P(Q)$] for monodispersed spherical primary particles with corresponding R_g values of 27, 50 and 104 Å (inset to Fig. 2) indicate that the primary particles exist as small aggregates that form the first length scale. Another common feature in the SAS data of all the composites, obtained using the USAXS instrument, is the occurrence of inter-particle correlations at high filler concentration at the longest length scale. This is illustrated in the log–log plots of the USAXS data for the 83 kDa PVAc composites with 2.5 and 12.5 vol.% NT-380 in Fig. 2: As expected the intensity at $Q > 0.001$ Å^{-1} for the 12.5 vol.% sample is higher than 2.5 vol.% however, at $Q = 0.001$ Å^{-1} the curves

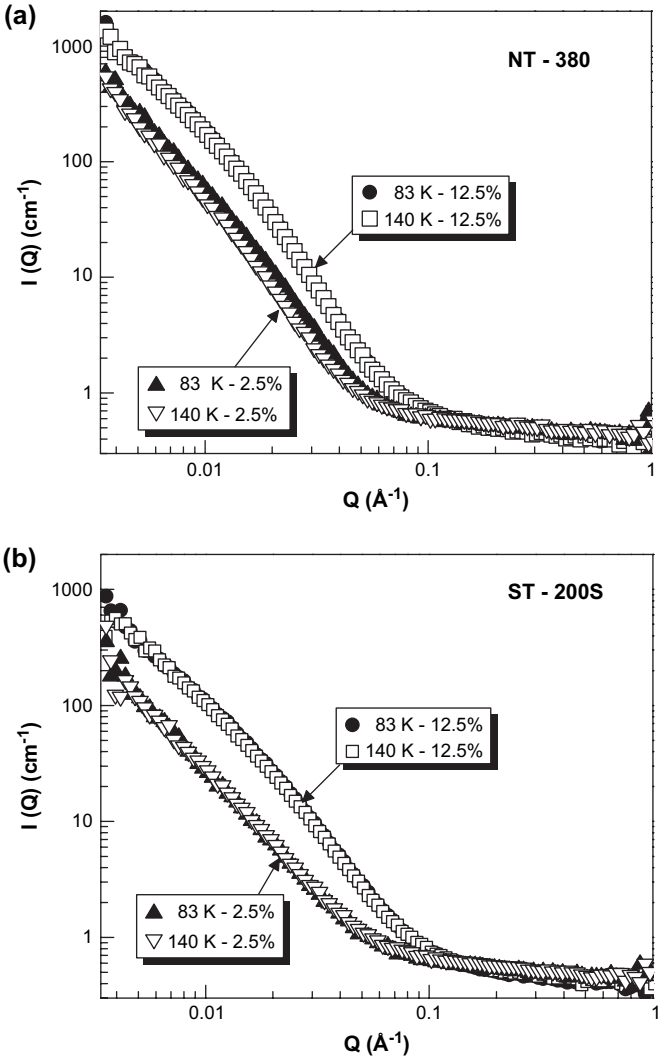

Fig. 1. SANS data at two filler concentrations (2.5 and 12.5 vol.%) and two matrix molecular weights (83 and 140 kDa) for the composites containing (a) NT-380 filler, and (b) ST-200S filler. Note that matrix MW has no appreciable effect on the scattering data for each concentration.

crossover. This deviation from scaling with the filler concentration at $Q < 0.004$ Å^{-1} for the 12.5 vol.% sample indicates the presence of inter-particle correlations at the agglomerate level. Therefore, to elucidate the structural features in the widest length scale without the effects of inter-particle correlations, we consider only the scattering data from the composites with 2.5 vol.% fillers for further analysis.

Figs. 3 and 4 present the log–log plots of USAXS data of the polymer nanocomposites corresponding to polymer MW of 83 kDa containing 2.5 vol.% NT and ST silica nanoparticles, respectively. We derived the particle size distribution for all the samples from a nonlinear least-square fitting [18] of $I(Q)$ [Eq. (1)] by assuming the form factor for a spherical particle and a log-normal distribution of particle sizes. To obtain the best fits we required two populations of scatterers. We also performed a similar particle distribution analysis for the composites containing 12.5 vol.% using the scattering data at $Q > 0.004$ Å^{-1}. The insets to Figs. 3 and 4 show the derived

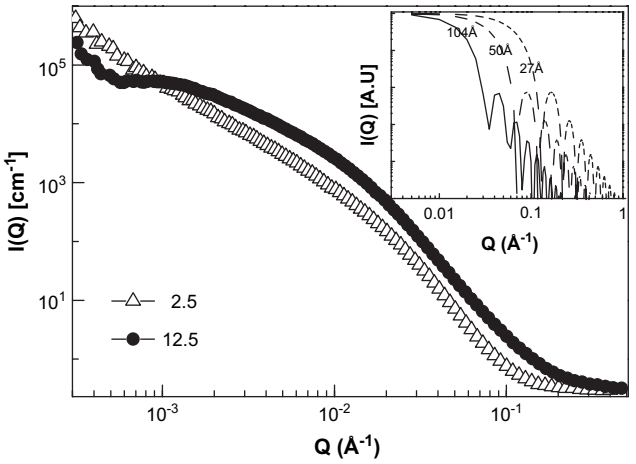

Fig. 2. $I(Q)$ versus Q for the NT-380 particles for 2.5 and 12.5 vol.% of silica. The crossover of the data at $Q \sim 0.001$ Å^{-1} for the 12.5 vol.% silica composite indicates the presence of strong inter-particle correlations between the large length scale objects. The inset shows log–log plot of the theoretically calculated form factors $[P(Q)]$ versus Q, for the three primary spherical particles. This indicates that the primary particles exist as aggregates in the composites.

particle volume distribution $V(D)$ as a function of the particle diameter D for the untreated and chemically treated composites with 2.5 vol.% filler, respectively. This is the envelope of the total distribution and it contains the peaks from both the population. The first peak is so overwhelming that the second peak is suppressed, nevertheless, this is the reason for the long tail in the distribution at larger diameters. We note that, in general, the fits at the lower Qs (Figs. 3 and 4) are not good leading to larger uncertainty in the parameters of the second population. This is because apart from the second population, there is a third population of agglomerates at $Q < 0.0007$ Å^{-1}. We only observe the power-law scattering from these agglomerates at the lowest Qs and the data is

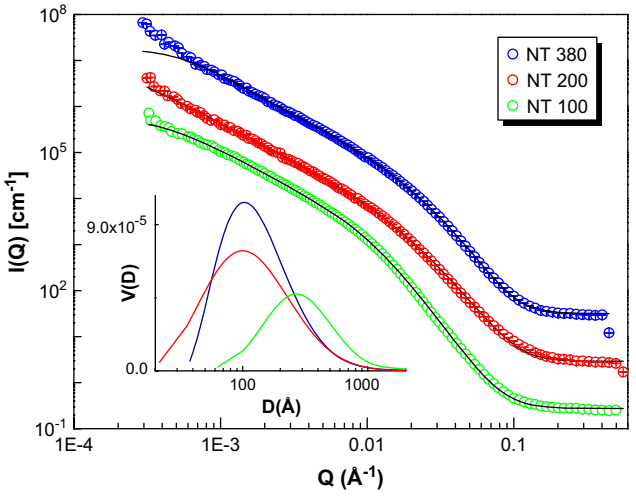

Fig. 3. USAXS data for the NT silica particles containing 2.5 vol.% of silica. The curves for NT-380 and NT-200 have been arbitrarily shifted for clarity by multiplying intensities by 10^2 and 10, respectively. The black lines are the fits to obtain the particle size distributions shown as an inset. For a given filler type the particle size distribution (see Table 1) is similar for composites with 2.5 and 12.5 vol.% filler loadings.

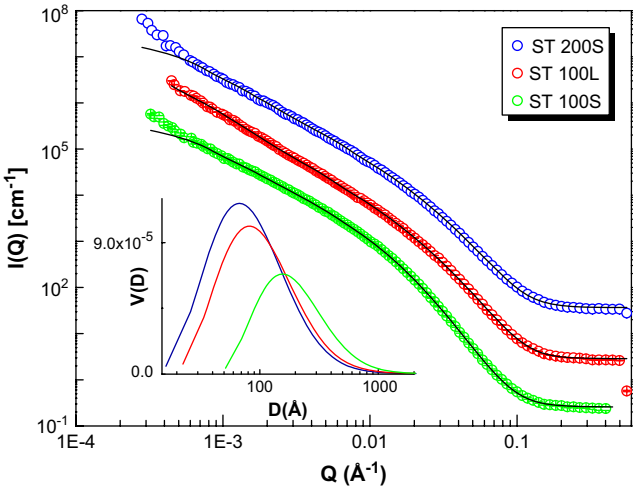

Fig. 4. USAXS data for the ST silica particles containing 2.5 vol.%. The curves for ST-200S and ST-100L have been arbitrarily shifted for clarity by multiplying intensities by 10^2 and 10, respectively. The black lines are the fits to obtain the particle size distributions shown as an inset. For a given filler type the particle size distribution (see Table 1) is similar for composites with 2.5 and 12.5 vol.% filler loadings.

limited by the accessible minimum Q. Therefore, in Table 1 we present the mean particle sizes and full-width-half-maximum (FWHM) of the first population in the distribution for all the samples. The fact that for a given filler type, the particle size and the FWHM in Table 1 for both 2.5 and 12.5 vol.% composites are similar implies that particle–polymer interactions at the interfaces are the same at both loadings. Focusing on the mean diameter D_1 in Table 1 and Fig. 3, we observe that the aggregate size monotonically decreases as the surface area increases, which is consistent with the correlation between the primary particle radius and the surface area.

The stronger effect of surface coating of particles on their aggregation is illustrated in Fig. 4. Again, focusing on D_1 and the overall particle size distribution, we can see that the particle aggregation in the composites is in the following order: ST-100L < ST-100S < NT-100, and also ST-200S < NT-200. It appears that the hydrogen bonding between the silica nanoparticles and the polymer in the case of the NT-100 filler is *not* sufficiently strong to prevent aggregation of nanoparticles. On the other hand, the long PDMS chain-tethered ST-100L filler, presumably through greater entanglement with

Table 1
Mean particle sizes (D_1) and their corresponding full-width at half-maximum (FWHM$_1$) belonging to the first level obtained from the size distribution analysis of the USAXS data for NT and ST silica particles in the PVAc matrix

Sample	2.5 vol.%		12.5 vol.%	
	D_1 (Å)	FWHM$_1$ (Å)	D_1 (Å)	FWHM$_1$ (Å)
100	394	435	409	465
100S	249	284	244	277
100L	153	172	151	173
200	201	228	182	208
200S	129	146	126	145
380	167	189	179	204

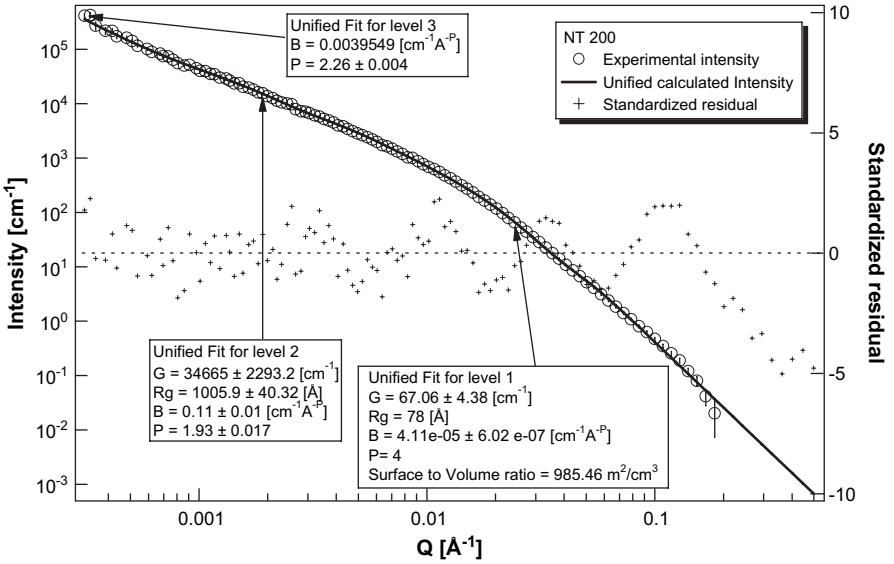

Fig. 5. Unified least-square fit to the USAXS data of 2.5 vol.% NT 200 silica in PVAc. The fit assumes three structural levels consisting of aggregates and agglomerates. In all the cases, primary particles are aggregated and thus we do not see their presence in the scattering data in the high Q region.

the polymer matrix (also the most hydrophobic coating, with all OH species blocked), exhibits the least aggregation of the particles. It is noteworthy that the ST-100L filler composites exhibit significantly different modulus recovery kinetics following a large strain perturbation when compared to the composites made with any other filler, either surface treated or untreated [8]. It thus appears that the attachment mechanism between filler and matrix, which in the case of ST-100L filler is by inter-diffusion of surface-tethered chains and matrix chains, alters both the initial tendency to aggregate and the modulus recovery process.

In order to characterize the hierarchical particle structure, we employed the unified fit method [13] of Beaucage (Fig. 5) to analyze the USAXS data for 2.5 vol.% samples. The gentle knee around $Q = 0.01$ Å^{-1} separates two structural levels: for $Q > 0.01$ Å^{-1} the main contribution to $I(Q)$ is from the particle aggregates that constitute the first structural level. The data at $Q < 0.01$ Å^{-1} is from the second structural level constituting larger aggregates. A third length scale seen as a power-law slope, could also be observed at the lowest Qs, pertaining to agglomerates whose size is beyond the instrument resolution. We earlier mentioned that the particle size distribution is accurate for the smaller particle. Therefore, while performing the unified fit, we fixed the particle size for the first level, for consistency, and varied the parameters in the second and third levels. The least-square unified fit parameters are collected in Table 2. We do not present the parameters for the third level, as due to the limited number of points, the parameters are not reliable. In level 1, P_1 is 4 for all the NT samples, and it is nearly 4 for the ST samples, implying a smooth and sharp particle–PVAc interface. The presence of Porod scattering enables the determination of the surface to volume ratio (A/V) for all samples (see Table 2). As expected, we observe that with surface treatment the A/V ratio increases due to better dispersion of the particles.

At the second structural level, we note that the trend in R_{g2} is similar to R_{g1}. The power-law exponent P_2 has values less than or equal to 2 for the NT composites, indicating the formation of chain-like mass-fractal aggregates. In particular, these values suggest that the growth mechanism of these mass-fractal aggregates is through cluster–cluster aggregation, [19] for which computer simulations have shown exponents between 1.75 and 2.05 as opposed to diffusion-limited aggregation [20] which would correspond to an exponent of 2.39 in three dimensions. Furthermore, the TEM image of the NT-380 sample (Fig. 6) corroborates this conclusion. Image analysis of TEM also provides a power-law slope of 1.78 ± 0.04 (Fig. 7) that agrees reasonably well with the mass-fractal

Table 2
Unified fit parameters for the USAXS data of 2.5 vol.% NT and ST silica particles in the PVAc matrix (the errors in the parameters are within 5%)

Sample	Level 1					Level 2				A
	G_1 (cm^{-1})	R_{g1} (Å)	B_1 (cm^{-1} Å^{-P})	P_1	A/V (m^2/cm^3)	G_2 (cm^{-1})	R_{g2} (Å)	B_2 (cm^{-1} Å^{-P})	P_2	
100	1168	153	1.9e − 05	4	367	1.4e + 05	1320	0.16	2.01	1.06
100S	277	96	3.0e − 05	4	589	3.9e + 04	845	0.04	2.23	1.64
100L	88	67	5.1e − 05	4	927	1.7e + 04	700	0.02	2.23	1.23
200	67	78	4.1e − 05	4	985	3.5e + 04	1006	0.11	1.93	1.00
200S	27	50	7.1e − 05	4	1403	0.9e + 04	582	0.03	2.13	1.25
380	63	65	4.8e − 05	4	1013	3.0e + 04	899	0.08	2.00	1.08

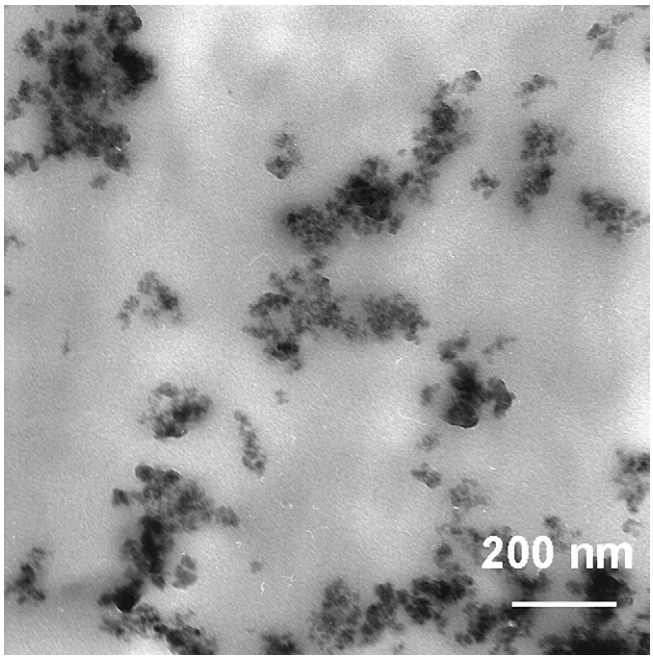

Fig. 6. TEM image of 2.5 vol.% NT-380/PVAc (83 kDa) showing the different aggregate sizes present in the composite.

nature of the aggregates. The difference in the power-law exponents between the TEM and USAXS may be due to the order of magnitude difference in sampling volumes of these two techniques. Interestingly, the power-law exponent is bigger for the ST particles. Increase in P_2, here, suggests a branching of the mass-fractal aggregates or increase in their polydispersity. The TEM image in Fig. 6 supports the latter. The parameter A in Table 2 calculated using the unified fit parameters in level 2, provides a measure of the polydispersity of the particle aggregates [17]. For the composites considered, A is mostly greater than 1, indicating the presence of linear polydispersed particle aggregates in the PVAc matrix. Interestingly, for the ST particles, it seems A is inversely related to R_{g2}. In general, a smaller R_{g2} would aid mechanical reinforcement and a larger A would

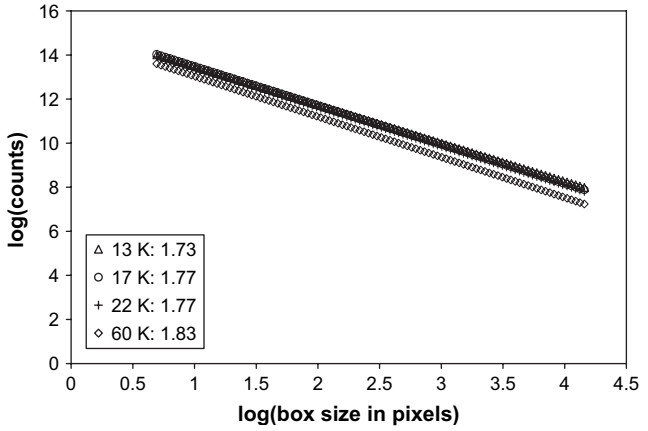

Fig. 7. Fractal dimensions calculated from TEM images. The legend indicates the image magnification and the fractal dimension calculated from the slope of the line. The average fractal dimension is 1.78 ± 0.04.

increase mechanical inhomogeneity, thus reducing reinforcement [21]. With the hypothesis that an ideal balance between A and R_g is required for mechanical reinforcement, let us look at the parameters for the ST composites. The ST-100S sample has the largest A and a considerably higher R_{g2}, and for a given filler concentration, has the highest loss factor as a function of shear strain amplitude, implying poor reinforcement characteristics [22]. Consider ST-200S and ST-100L, which have nearly the same A, but the R_{g2} of ST-200S is smaller than ST-100L. Yet, the loss factor for the ST-100L is the lowest among all the samples, implying the best mechanical reinforcement. The loss factor gradually increases with strain amplitude and overtakes NT particles at about 5% strain [22]. Such an increase in loss factor with strain amplitude is attributed to the release of trapped chain formations at the particle surface. The loss factor for ST-200S overtakes all other samples even at 2% strain [22]. Contrary to the belief, the smaller R_{g2} of ST-200S, which is consistent with the high particle surface area in Level 1 (Table 2), provides an explanation. Usually, a large particle surface area implies a greater interaction with the matrix polymer. However, in the ST-200S sample, the surface treatment with a small molecule (not a polymer) prevents not only hydrogen bonding with the matrix, but also precludes entanglement with the matrix polymer.

We summarize the USAXS data analysis with the following picture on the particle arrangement which is similar to the structure proposed for random porous materials [14], except that the 'pores' here are replaced by the matrix polymer: the particles in the backbone of the network is made up of aggregates whose size is characterized by R_{g1}, and whose surface is nearly smooth. These particles string together to form linear polydispersed mass-fractal aggregates of size R_{g2}. These aggregates further associate to form agglomerates.

Before we conclude, a remark on the origin of aggregation is in order. Recently, it has been shown [23] by thermodynamic considerations, that when the R_g of the linear polymer exceeds the nanoparticle radius, dispersion of the nanoparticle is promoted. The R_g of PVAc for the molecular weights 83 and 140 kDa can be estimated [24] to be 94 and 122 Å, respectively. These values exceed the nanoparticle radius except for the particle with the smallest surface area corresponding to a radius of 135 Å. Although in all the samples we observe particle aggregation, there is a definite trend towards lesser aggregation with decrease in nanoparticle radius, which is consistent with the above picture. In the future, it may be useful to understand the role of particle surface treatment in this context.

4. Conclusions

The SANS results show that changes in aggregation state cannot be used to explain the changes in reinforcement when different MW matrices are employed, especially when the filler and polymer are strongly attracted to each other. Thus, at low filler concentrations it appears that formation of a transient polymer–particle network arising due to the nature of filler–polymer interactions [7] is a viable explanation for the

high reinforcement. However, this mechanism is likely to be competitive (act in concert) with aggregation/agglomeration mechanisms especially at higher filler concentrations. Filler–polymer interactions may also provide explanations of phenomena otherwise not easily treated with aggregation models, for example, the absence of a static strain effect on the dynamic modulus behavior with strain amplitude [9]. Experimental data to be submitted for publication in the near future [25] demonstrate that the addition of fillers to polymer melts results in the addition of longer relaxation times to the matrix behavior and that this addition is greater for higher filler–matrix interaction energies and for higher filler concentrations.

The USAXS data and the TEM picture show that filler particles form linear polydispersed aggregates. Polydispersity increases mechanical inhomogeneity and possibly alters the mechanical reinforcement characteristics of the polymer matrix by the filler. Future experiments will focus on USAXS studies at temperatures above the glass transition temperature, leading to better comparisons with the existing viscoelastic measurements [7,8]. The relative contributions of filler aggregation and filler–polymer interactions (as related to chain conformation restrictions) to the reinforcement mechanism at low volume fractions remains an open question, and it is likely that both play roles depending on the filler's concentration, size and surface characteristics, the filler–polymer interaction energies, matrix MW, and composite processing procedures.

Acknowledgements

We thank Prof. G. Beaucage (University of Cincinnati) for useful discussions. This work was supported by the Nanoscale Science and Engineering Initiative of the National Science Foundation under NSF award numbers DMR-0117792, DMR-0413755 and CTS-9871894 and by the Office of Naval Research under grant number N00014-99-1-0187. The UNICAT facility at the Advanced Photon Source (APS) is supported by the University of Illinois at Urbana-Champaign, Materials Research Laboratory (U.S. DOE, the State of Illinois-IBHE-HECA, and the NSF), the Oak Ridge National Laboratory (U.S. DOE under contract with UT-Battelle LLC), the National Institute of Standards and Technology (U.S. Department of Commerce) and UOP LLC. Argonne National Laboratory's work was supported by the U.S. Department of Energy, Office of Science, Office of BES under contract DE-AC02-06CH11357 to U. Chicago, Argonne LLC. R.A.N acknowledges the support by the Office of BER research of the US DOE under contract no. DE-AC05-00OR22725 with Oak Ridge National Laboratory managed and operated by UT-Batelle, LLC.

References

[1] Jordan J, Jacob KI, Tannenbaum R, Sharaf MA, Jasuik I. Mater Sci Eng A 2005;393:1–11.
[2] Hergeth W, Steinau U, Bittrich H, Simon G, Schmutzler K. Polymer 1989;30:254–8.
[3] Iisaka K, Shibayama K. J Appl Polym Sci 1978;22:3135–43.
[4] Payne AR. J Appl Polym Sci 1965;9:2273–84.
[5] Heinrich G, Kluppel M. Adv Polym Sci 2002;160:1–44.
[6] Maier PG, Goritz D. Kautsch Gummi Kunstst 1996;49:18.
[7] Sternstein SS, Zhu A-J. Macromolecules 2002;35:7262–73.
[8] Zhu A-J, Sternstein SS. Comp Sci Technol 2003;63:1113–26.
[9] Chazeau L, Brown JD, Yanyo LC, Sternstein SS. Polym Compos 2000;21:202–22.
[10] Thiyagarajan P, Urban V, Littrell K, Ku C, Wozniak DG, Belch H, et al. In: Carpenter JM, Tobin C, editors. Proceedings of the ICANS XIV, June 14–19, 1998, Starved Rock Lodge, Utica, Illinois, vol. 2. Springfield, VA: National Technical Information; 1998. p. 864–78.
[11] Ilavsky J, Allen AJ, Long GG, Jemian PR. Rev Sci Instrum 2002; 73:1660.
[12] Roe R-J. Methods of X-ray and neutron scattering in polymer science. Oxford: Oxford University Press; 2000.
[13] Beaucage G. J Appl Crystallogr 1995;28:717–28.
[14] Schaefer DW, Keefer KD. Phys Rev Lett 1986;56:2199–202.
[15] Porod G. In: Glatter O, Kratky O, editors. Small angle X-ray scattering. New York: Academic; 1982.
[16] Beaucage G, Kammler HK, Pratsinis SE. J Appl Crystallogr 2004; 37:523–35.
[17] Beaucage G. Phys Rev E 2004;70:031401.
[18] Ilavsky, J. Irena 1 SAS modeling software, <www.uni.aps.anl.gov/~ilavsky/irena.html>.
[19] Meakin P. In: Family F, Landau P, editors. Kinetics of aggregation and gelation. New York: North-Holland; 1984;
Kolb M, Botet R, Jullien J. Phys Rev Lett 1983;51:1123–6.
[20] Witten TA, Sander LM. Phys Rev Lett 1981;47:1400–3;
Sander LM, Cheng ZM, Richter R. Phys Rev B 1983;28:6394–6.
[21] Papakonstantopoulos GJ, Yoshimoto K, Doxastakis M, Nealey PF, de Pablo JJ. Phys Rev E 2005;72:031801.
[22] Zhu A-J, Sternstein SS. Mat Res Soc Symp Proc 2001;661:KK4.3.1–KK4.3.7.
[23] Mackay ME, Tuteja A, Duxbury PM, Hawker CJ, Horn BV, Guan Z, et al. Science 2006;311:1740–3.
[24] Chan R, Worman C. Polym Eng Sci 1972;12:437–43.
[25] Shofner ML, Ozisik R, Schadler L, Sternstein SS. In preparation.